



Aeropropulsive Design Optimization of a Boundary Layer Ingestion System

Anil Yildirim*

University of Michigan, Ann Arbor, MI, 48109, U.S.A.

Justin S. Gray†

NASA Glenn Research Center, Cleveland, OH, 44135, U.S.A.

Charles A. Mader‡ and Joaquim R. R. A. Martins§

University of Michigan, Ann Arbor, MI, 48109, U.S.A.

Boundary layer ingestion (BLI) is a technology where the main propulsion system or an auxiliary fan is used to ingest the wake generated by the aircraft to improve aeropropulsive performance. The STARC-ABL concept introduced by NASA uses this technology with a traditional tube and wing configuration. Even though the concept is similar to conventional aircraft, design intuition is heavily limited due to the lack of previous experience with BLI. To achieve energy savings through BLI, multidisciplinary analysis and optimization tools that consider the fully coupled aeropropulsive design are required. In this work, we optimize the BLI system design of the STARC-ABL configuration at a number of net force and fan pressure ratio (FPR) values using a coupled aeropropulsive approach. The optimized designs demonstrate the increase in shaft power requirement for the BLI fan with increasing FPR values. We show that the power requirement is more sensitive to the thrust required from the BLI system, while the stagnation pressure distribution at the wake is more sensitive to FPR.

Nomenclature

| | |
|-------------------------|---|
| $(\cdot)^{\text{aero}}$ | = value in the aerodynamic model |
| $(\cdot)^{\text{prop}}$ | = value in the propulsion model |
| $(\cdot)^*$ | = target value in optimization problems |
| $(\cdot)_{\infty}$ | = free-stream quantity |
| $(\cdot)_t$ | = total quantity |
| $(\cdot)^{\text{ref}}$ | = reference quantity |
| A | = area |
| α | = angle of attack |
| C_{fx} | = coefficient of net force in the x direction |
| C_L | = coefficient of lift |
| C_p | = coefficient of pressure |
| \hat{e}_x | = unit vector in the x direction |
| FPR | = fan pressure ratio |
| \vec{f} | = force vector |
| \vec{f}_{visc} | = viscous force vector |
| \vec{F}_{BLI} | = force vector applied in the fan model |
| g_{geo} | = geometric thickness constraints |
| h | = enthalpy |
| M | = Mach number |
| \dot{m} | = mass flow rate |

*Ph.D. Candidate, Department of Aerospace Engineering, AIAA Student Member

†Research Engineer, Propulsion Systems Analysis Branch, AIAA Member

‡Assistant Research Scientist, Department of Aerospace Engineering, AIAA Senior Member

§Professor, Department of Aerospace Engineering, AIAA Associate Fellow

| | | |
|----------------------------------|---|---|
| \hat{n} | = | surface normal vector |
| p | = | pressure |
| p_s | = | static pressure |
| PSC | = | power saving coefficient |
| $\mathcal{P}_{\text{shaft}}$ | = | shaft power |
| $\mathcal{P}_{\text{flow}}$ | = | power added to the flow |
| $\mathcal{P}_{\text{shaft-BLI}}$ | = | shaft power required to operate the BLI fan |
| \mathcal{R} | = | residual function |
| ρ | = | density |
| T | = | temperature |
| V | = | velocity |
| X_{shape} | = | shape design variables |

I. Introduction

Boundary layer ingestion (BLI) is a concept where aerodynamic and propulsive performance gains are obtained by using propulsors that ingest the boundary layer generated by the passive surfaces of an aircraft, such as the fuselage. Despite being around for some time, BLI technology has not been utilized in a practical aircraft configuration because of the limitations in the design tools required to fully take advantage of BLI. Furthermore, traditional thrust and drag accounting approaches cannot be utilized with configurations utilizing BLI due to the integrated nature of the propulsion system to the geometry [1]. One of the first studies of wake ingestion related to aircraft propulsion was done by Smith [2]. In this work, to quantify the benefits of BLI, the metric power saving coefficient (PSC) was defined as

$$\text{PSC} = \frac{\mathcal{P}_{\text{shaft}} - \mathcal{P}_{\text{shaft-BLI}}}{\mathcal{P}_{\text{shaft}}}, \quad (1)$$

which represents the reduction in the power requirements for a configuration utilizing BLI ($\mathcal{P}_{\text{shaft-BLI}}$) compared to a reference podded configuration ($\mathcal{P}_{\text{shaft}}$) to achieve the same net force coefficient on the overall body. Similarly, Drela [3] developed the power balance method to address the challenges regarding BLI theory.

Recently, NASA introduced the STARC-ABL concept [4], where a propulsor mounted on the tail cone of a conventional tube and wing configuration is used to ingest the boundary layer generated by the fuselage to improve aeropropulsive performance, as visualized in Figure 1. Even though the configuration is very similar to conventional aircraft, existing engineering intuition is heavily limited due to the emergent BLI technology. Therefore, to accurately quantify the benefits of BLI with this configuration, preliminary design studies are required.

There are a number of recent studies that built the framework necessary to perform design optimization with the STARC-ABL configuration. Hall et al. [5] developed a 3-D fan model that preserves the flow properties such as inlet distortion to study BLI. Gray and Martins [6] performed a series of aeropropulsive optimizations to quantify the benefits of BLI by calculating the PSC values for a range of net force coefficients on the combined fuselage and propulsor configuration. This study focused on a two dimensional axisymmetric formulation, and two configurations were optimized for each target force coefficient: one configuration where the fan is mounted on the aft fuselage, and a reference configuration with a clean fuselage and a podded propulsor. They concluded that fully coupled aeropropulsive design methods are required to maximize the benefits from BLI. Gray et al. [7] extended their previous work to a three dimensional configuration to capture the non-axisymmetric effects caused by the fuselage and the wings. They found that enforcing a constraint on inlet distortion of the fan face reduced the benefits of BLI and the tradeoff between inlet distortion and BLI benefits must be studied further. Kenway and Kiris [8] performed a series of optimizations with the STARC-ABL configuration to minimize the inlet distortion on the BLI fan face. They discovered that the downwash from the wings contribute to the fan face distortion and stated that inclusion of the wings in the models are required to compute the fan face distortion accurately.

In this work, we build upon the methodology developed by Gray [9] and perform a number of optimizations with the full three dimensional configuration. These optimization problems target a sweep of net force and fan pressure ratio (FPR) values with the STARC-ABL configuration. With the results from these optimizations, we quantify the shaft power requirements for the BLI fan throughout the design space. In the remainder of this document, we describe our methodology, define the optimization problems we consider, and present the results from this design study.



Fig. 1 Rendering of the STARC–ABL configuration. The tail-cone thruster ingests the fuselage boundary layer to improve aeropropulsive efficiency.

II. Methodology

BLI is an aeropropulsive concept that relies on synergistic interactions between the fuselage aerodynamics and the thrust producing turbomachinery. Gray et al. [10] used a coupled aeropropulsive model of the STARC–ABL configuration, with 2-D RANS CFD for the aerodynamics and a 1-D thermodynamic cycle model for the propulsion, to show that aerodynamic and propulsive effects contributed equally to the overall BLI performance gains. Therefore, in order to accurately model the performance of BLI systems, it is crucial to use a fully coupled aeropropulsive model, which accounts for the reciprocal interactions between the two disciplines. We use OpenMDAO [11] to build our coupled aeropropulsive framework, and in this section, we describe the components in this coupled model.

A. Geometry Parametrization and Mesh Warping

For geometry parametrization and manipulation, we use OpenVSP [12], which is a parametric geometry tool for aircraft preliminary design. OpenVSP uses *components* as building blocks to represent aircraft geometries, and a geometry model in OpenVSP contains the continuous representations of the component surfaces using Bézier curves and surfaces. The baseline OpenVSP model of the STARC–ABL configuration contains multiple components such as the fuselage, wing, vertical stabilizer, and the BLI nacelle, as shown in Figure 2. In this work, we omit the under-wing engines and horizontal stabilizers from the model for simplicity. In the optimization problems we consider herein, we include design variables to modify the aft fuselage and BLI nacelle geometries. The parametrization of these surfaces use human readable design variables, such as cross section diameters and tangent angles, as shown in Figure 3.

The main challenge of using OpenVSP as the geometry manipulation tool with high-fidelity design optimization is propagating the changes in the design of the continuous surface representations in OpenVSP, to the discrete surface nodes of the CFD mesh. Around regions that are defined by a single component in OpenVSP, this can be achieved by projecting the CFD surface nodes on the continuous surfaces, and tracking the parametric coordinates of these projected points throughout the optimization process. The component for each CFD surface node is determined by proximity; we select the component that yields the smallest projection distance for each node. These projections can be done directly within the Python interface of OpenVSP; therefore, this process is not limiting in terms of performance. Because the CFD surface mesh is built directly with the geometry obtained from the OpenVSP model, the projection distances for the CFD nodes are typically on the order of the numerical accuracy of the meshing tool. As a result, we directly link the surface nodes of the CFD mesh with the projected points on the OpenVSP geometry, and move the CFD surface nodes by the same amount the projected points move as the design changes.

This approach is suitable to regions of the aircraft surface that are away from intersections of two OpenVSP components, but the regions close to component intersections require special handling. The geometry model we have in this work contains multiple intersections; however, the only intersection curve that gets affected by design changes is the one between the fuselage and the vertical stabilizer, shown in Figure 4a. Figure 4b presents a detailed view of the CFD

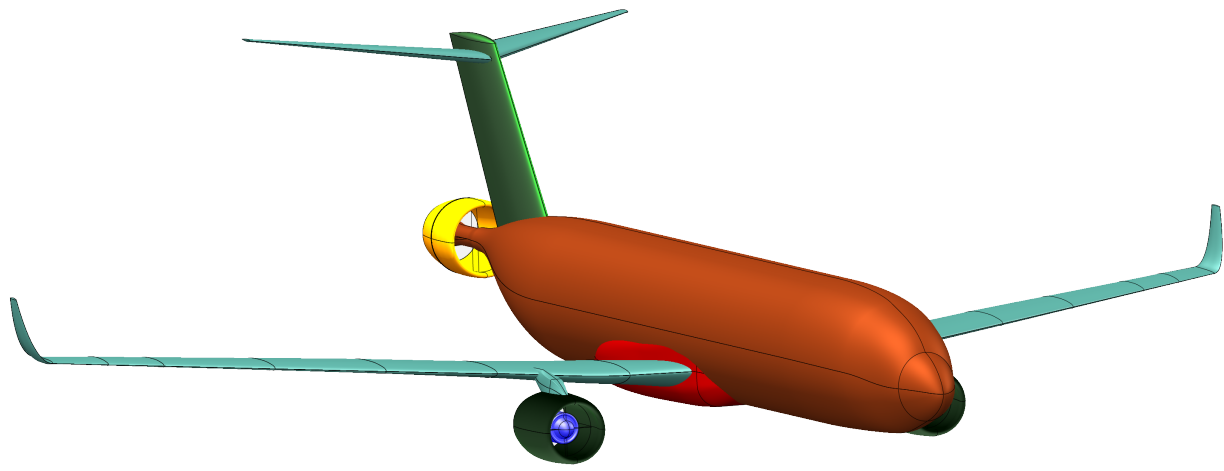


Fig. 2 OpenVSP model of the STARC–ABL configuration. Different colors are used to highlight different components in the geometry model. In this work, we omit the under-wing engines and horizontal stabilizers for simplicity.

surface nodes that are close to this intersection. Because we directly project the CFD surface nodes on the continuous surfaces, the nodes near intersections move with the surface projections. If we do not include the effects of the modified intersection on these nodes, geometry deformations can cause failures in the CFD surface mesh, as demonstrated in Figure 4c.

To accurately displace the CFD surface nodes around these intersections, we first need to track the intersection curves themselves as the design changes. To do so, along with the CFD surface nodes, we also project a set of surface triangulation nodes for each intersecting component and track these nodes along with the CFD surface nodes. After each design change, we compute the new intersection curves using the framework developed by Secco et al. [13]. For these computations, we use the triangulated surface meshes we track for each intersecting component. Then, we use an inverse-distance weighting method to warp the CFD surface nodes that are close to these intersections. This method displaces the CFD surface nodes that are on the intersections to track the intersection curves directly. The CFD surface nodes that are a certain distance away from the intersections are displaced by a weighted average of the intersection curve and surface projection displacements. As a result, the CFD surface mesh resolution around the intersections is preserved, while there is a smooth transition between the intersections and the surfaces away from the intersections. Figure 4d shows the result of this approach, and Figure 4e demonstrates how the CFD nodes near these intersections are displaced compared to the initial design.

Once we displace the surface nodes that define the CFD surface mesh after a design change, we use the mesh warping algorithm developed by Luke et al. [14] to propagate the changes of the surface nodes to the volume nodes of the CFD mesh. We use the open source mesh deformation tool IDWarp* to incorporate this mesh warping algorithm in our design framework.

B. Aerodynamic Model

The aerodynamic analyses are performed with the open source CFD solver, ADflow[†], which can solve RANS equations on structured multiblock and overset meshes. ADflow is especially well suited to optimization applications because of its extremely efficient adjoint solver implementation to obtain accurate derivatives [15].

The CFD simulations use an overset mesh that contains around six million cells and a symmetry plane about the middle of the aircraft. The coefficient of pressure contours obtained with the initial design, along with the active cells in the overset mesh are shown in Figure 5. Due to the challenging nature of the CFD model that contains an actuator region to model the BLI fan, we use the approximate Newton–Krylov solver implemented in ADflow [16].

*<https://github.com/mdolab/idwarp>, accessed May 2019

[†]<https://github.com/mdolab/adflow>, accessed May 2019

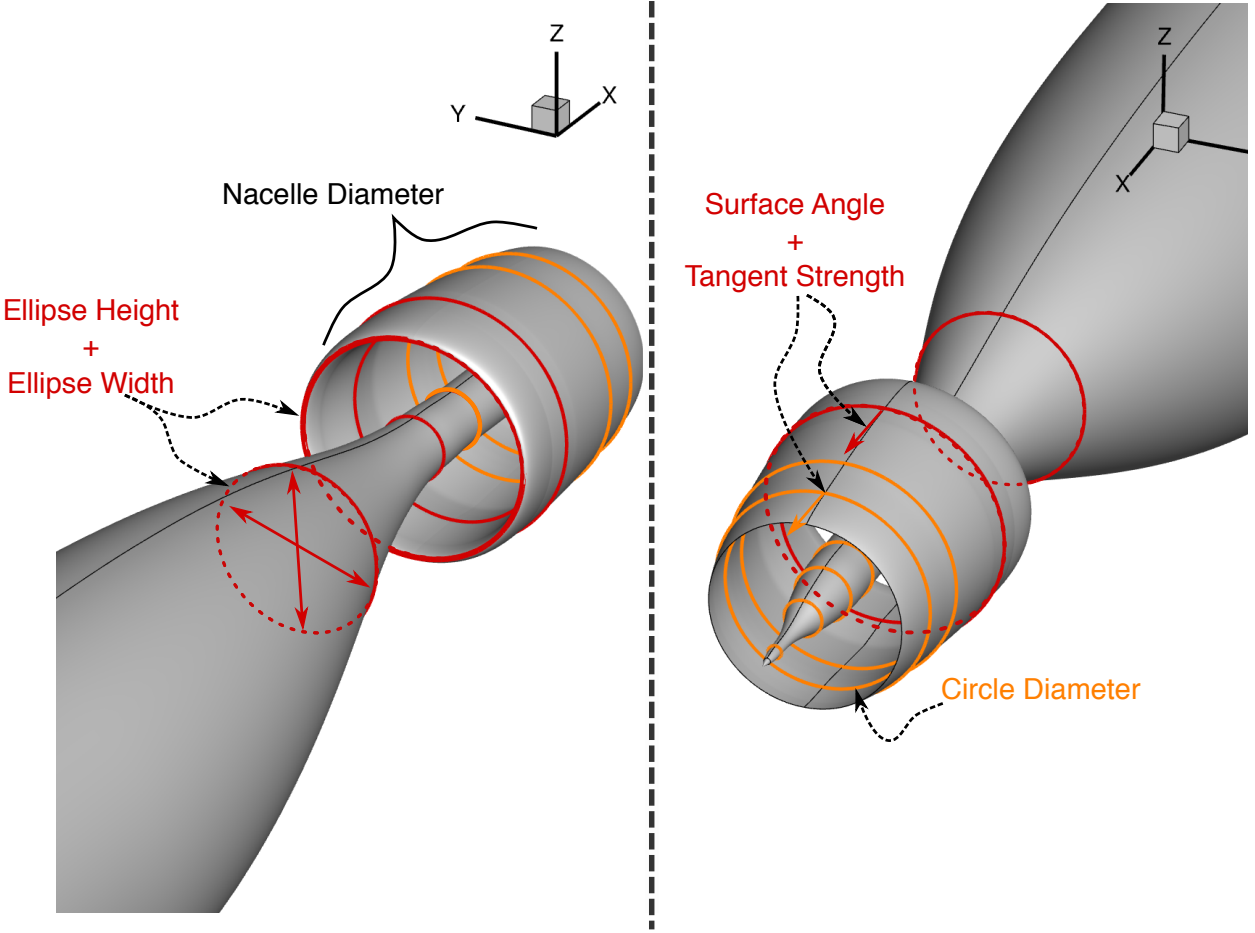


Fig. 3 Geometry parametrization. The vertical tail, which is present in the geometry model in this work, is not included in this figure for simplicity. The figure on the left demonstrates the design variables on the aft fuselage, and the diameter design variable to size the nacelle. The figure on the right highlights the cross sections on the nacelle geometry where we control the surface angle, tangent strength, and circle diameter.

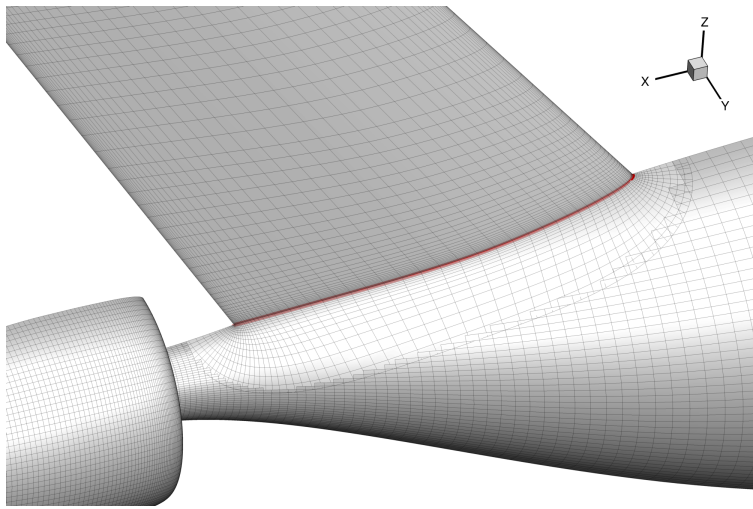
C. Propulsion Model

The propulsion model is split up in two parts that are handled separately in different solvers. The thrust produced is modeled using a simple axial actuator zone embedded within the CFD mesh, inside the aft-propulsor nacelle. The actuator zone is highlighted in Figure 6, along with the initial design of the aft section. Within the actuator zone, the axial force acting on the flow is divided in a volume weighted manner throughout CFD mesh cells inside the zone. This axial force represents the effect of the fan on the flow, and thus can be thought of as the net force that would be felt by a thrust bearing supporting the fan.

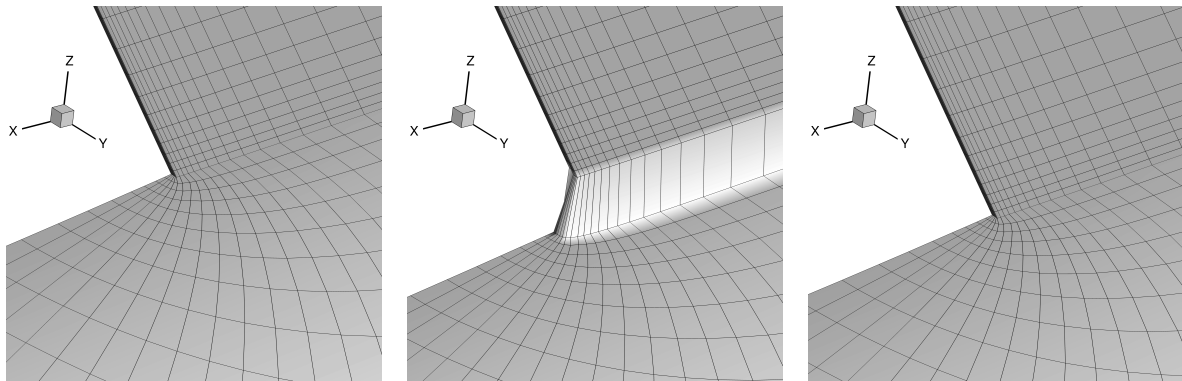
Force accounting in a configuration that uses BLI is not straightforward. Even for a standalone fan, the total thrust obtained is not equal to the amount of thrust distributed over the actuator region, as the pressure forces over a closed control volume needs to be integrated to accurately account for the net thrust. With the introduction of BLI, the definition of a closed control volume is not straightforward, therefore the traditional thrust and drag accounting schemes fall apart. Due to this, we use the net force coefficient in the x direction herein, written as

$$C_{fx} = \frac{2}{\rho_\infty V_\infty^2 A_{ref}} \left[\iint_S \left((p - p_\infty) \hat{n} + \vec{f}_{visc} \right) \cdot \hat{e}_x dS + \vec{F}_{BLI} \cdot \hat{e}_x \right], \quad (2)$$

where \hat{e}_x denotes the unit vector in the x direction of the aircraft frame of reference. For the STARC-ABL configuration the reference area A_{ref} is 105.8m^2 . The reference density ρ_∞ is 0.3506kg/m^3 and velocity V_∞ is 231.7m/s at cruise



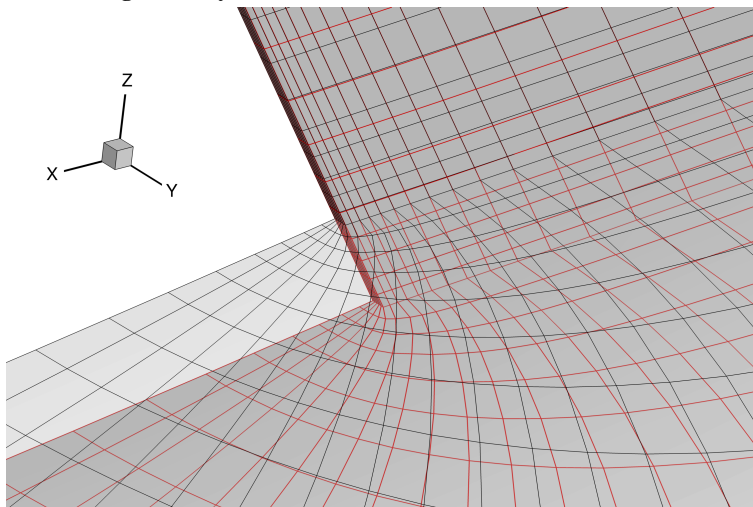
(a) Initial design. The intersection between the fuselage and vertical stabilizer is highlighted in red.



(b) Detailed view of the vertical tail trailing edge with the initial design.

(c) Modified surface mesh without any intersection treatment.

(d) Modified surface mesh after the intersection treatment.



(e) The CFD surface mesh near the intersection before and after the design change. Initial mesh is highlighted with black, while the modified mesh is highlighted in red.

Fig. 4 Effects of modifying component intersections to the CFD surface mesh. The surface nodes close to the intersections require special treatment with component based geometry tools.

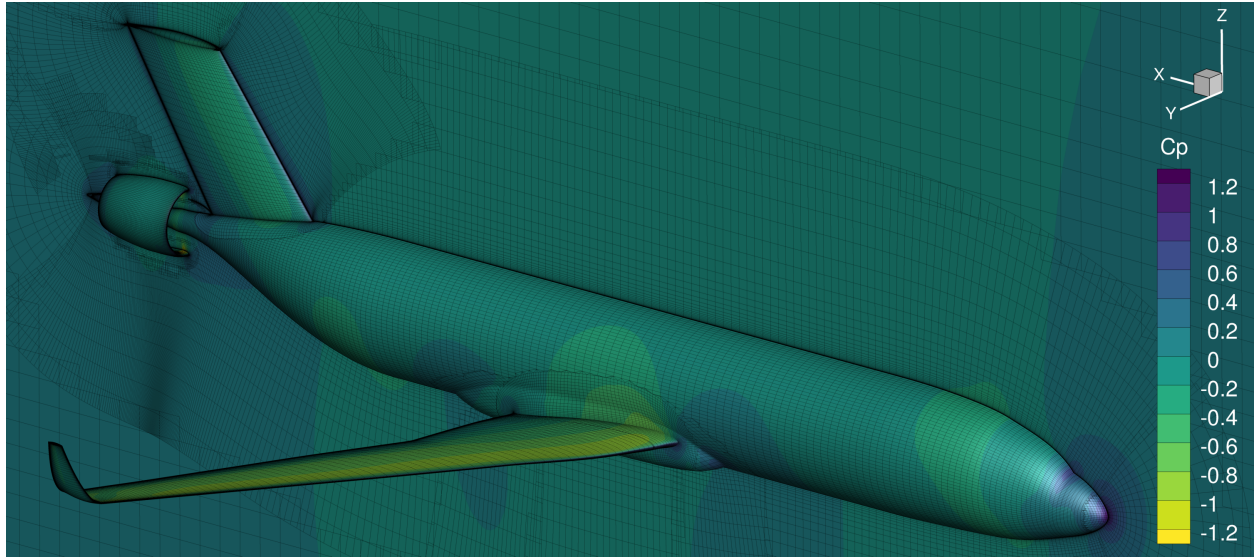


Fig. 5 Coefficient of pressure contours of the CFD solution using the initial design.

conditions of Mach number 0.785 and altitude 37 000 ft. With this formulation, a positive C_{fx} value means that there is a total net drag on the body, and this number represents the additional thrust required from the under-wing engines for the full configuration at steady flight, as we do not model the under-wing engines in this work.

Based on the thrust input and the velocity field in the actuator zone, the power added to the flow can be computed as

$$\mathcal{P}_{\text{flow}} = \iiint_V (\vec{V} \cdot \vec{f}) dv, \quad (3)$$

where \vec{V} and \vec{f} are the velocity and force vectors respectively, and the integration takes place over the volume that defines the actuator region. However, this simple formulation is isentropic and does not account for the adiabatic efficiency of the fan. When the adiabatic fan efficiency is taken into account, the actual shaft power required will be higher than the value computed with Eq. (3). To account for this, we use a 1-D thermodynamic model of the aft propulsor using the pyCycle modeling library [17, 18]. The inputs to this model include the fan pressure ratio, mass averaged fan-face velocity, and area averaged fan-face static pressure.

D. Aeropropulsive Coupling

The 1-D thermodynamic calculations for the second part of the propulsor model require total pressure, total temperature, mass flow rate, and Mach number. However, these quantities are not directly available from the CFD solution; therefore, some form of averaging is required to compute equivalent quantities from the 3-D flow field. Gray [9] developed a force based averaging scheme with the idea that the most consistent interface between the two codes is one that would have the same effective force on the fan face in both analyses. This scheme is given by the implicit relationships:

$$\begin{aligned} \mathcal{R}_p(p_t^{\text{prop}}) &= p_s^{\text{prop}} - p_s^{\text{aero}} = 0, \\ \mathcal{R}_T(T_t^{\text{prop}}) &= V^{\text{prop}} - V^{\text{aero}} = 0, \\ \mathcal{R}_M(M^{\text{prop}}) &= A^{\text{prop}} - A^{\text{aero}} = 0, \end{aligned} \quad (4)$$

where we define three residual equations that are equal to zero when the fan face static pressure (p_s), flow velocity (V), and fan-face area (A) values are equal between the aerodynamic and propulsion models. Eq. (4) requires the inputs values fan-face area, mass-averaged fan-face velocity, and area-averaged fan-face pressure to be computed by the CFD analysis. Then, within the 1-D thermodynamic analysis, a Newton solver is used to find the fan-face total pressure, fan-face total temperature, and Mach number that satisfy Eq. (4). Once the equivalent total properties have been computed, a standard 1-D compressor analysis can be performed to compute the shaft power, while accounting for the adiabatic efficiency. The overall model structure is shown as an XDSM diagram [19] in Figure 7.

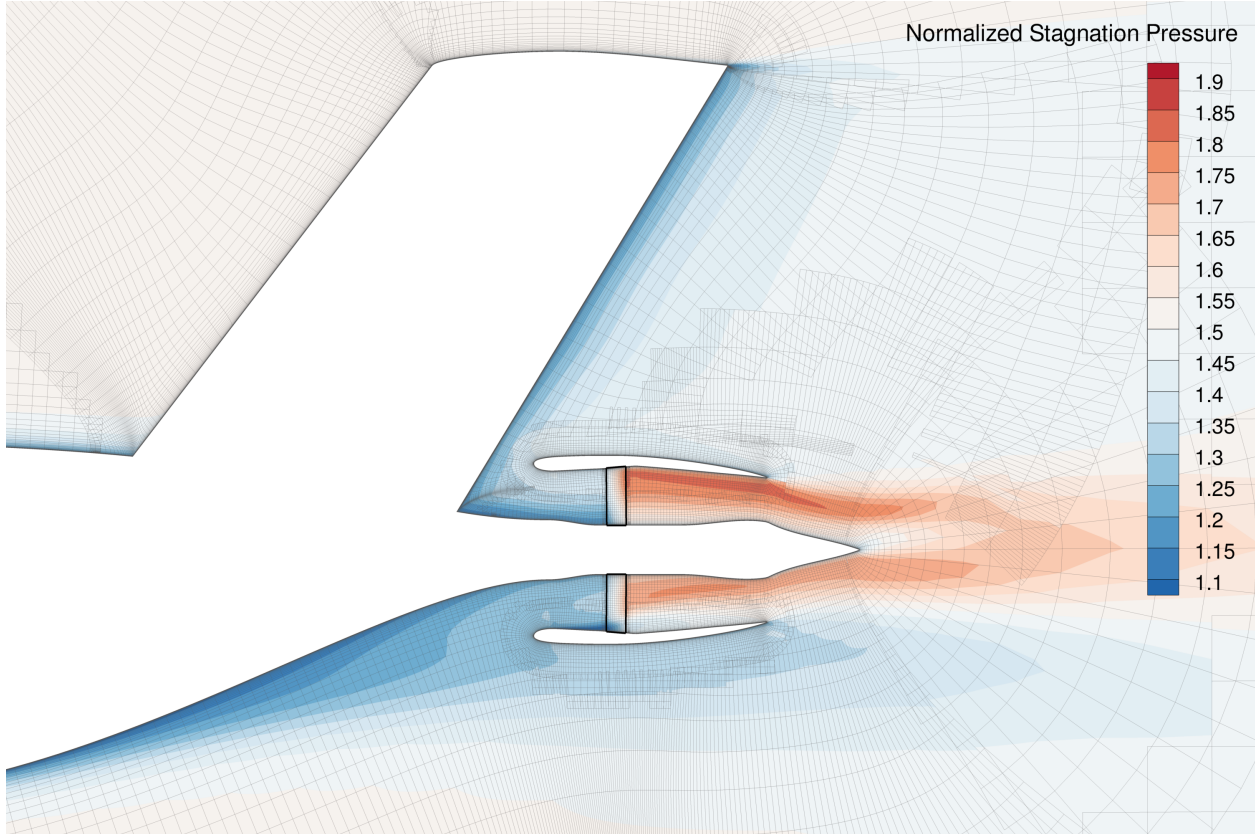


Fig. 6 Initial design of the aft section, viewed from the symmetry plane. The actuator region is highlighted in black frames, while the active cells in the overset mesh are shown in light gray. Stagnation pressure contours are normalized with respect to the free-stream static pressure. Blue color represents lower stagnation pressure, while red represents higher stagnation pressure compared to free stream.

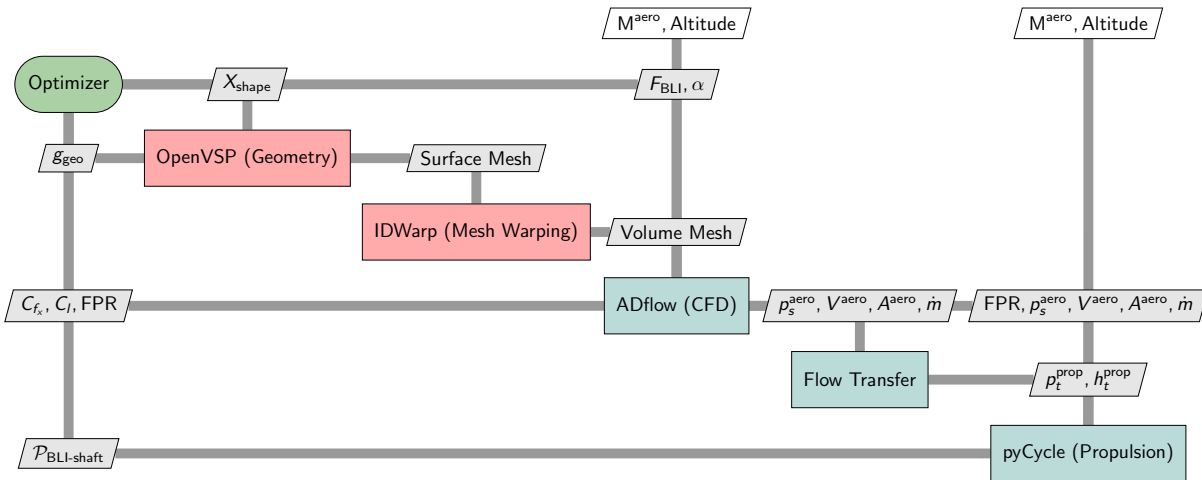


Fig. 7 XDSM diagram of the aeropropulsive design optimization framework. Explicit and implicit components are shown in red and blue respectively. The *Flow Transfer* component solves Eq. (4) for the force-based transfer scheme. Design variables are the geometry parameters (X_{shape}), BLI fan thrust (F_{BLI}), and angle of attack (α).

Table 1 Optimization problem definition. We have 27 design variables and 13 constraints.

| | Variable/Function | Description | Quantity |
|-----------------|------------------------|--|----------|
| minimize | $P_{BLI\text{-}shaft}$ | Shaft power required for the BLI fan | 1 |
| with respect to | α | Angle of attack | 1 |
| | F_{BLI} | The body force applied for the BLI fan | 1 |
| | X_{shape} | Shape variables for BLI fan nacelle and aft fuselage | 25 |
| | Total | | 27 |
| subject to | $C_{fx} = C_{fx}^*$ | Target force coefficient | 1 |
| | $FPR = FPR^*$ | Target FPR | 1 |
| | $C_L = 0.5$ | Lift coefficient at cruise | 1 |
| | $0.99 < g_{geo} < 3.0$ | Geometric thickness constraints | 10 |
| | Total | | 13 |

Table 2 Design parameters for each optimization problem. We perform optimizations with each combination of C_{fx} and FPR for a total of 9 optimizations.

| Parameter | Target values |
|----------------------|------------------|
| $C_{fx} \times 10^4$ | 90, 110, 130 |
| FPR | 1.25, 1.30, 1.35 |

III. Optimization Problem Definition

Thrust and drag are not well defined quantities for configurations using BLI because we cannot define closed control volumes for the integrations required to calculate these terms separately [3]. Therefore, we have to reformulate the typical aerodynamic shape optimization problem that usually aims to minimize an objective function that contains net drag. Therefore, we optimize for minimum shaft power required to operate the BLI fan, given a total net force constraint, among a number of other constraints. The optimization problem we solve is summarized in Table 1. In this work, we perform optimizations for combinations of three C_{fx} and FPR values each, which are listed in Table 2, for a total of nine optimizations. We use SNOPT [20] as the optimizer for these optimization problems, through the Python interface pyOpt [21].[‡]

The amount of thrust required from the under-wing engines is proportional to C_{fx} for steady flight. As a result, a smaller C_{fx} target is equivalent to having a smaller portion of the total thrust from the under-wing engines and a larger portion from the BLI fan, and therefore, we expect a higher shaft power requirement to operate the BLI fan. Conversely, a larger C_{fx} value represents designs where the under-wing engines need to provide more thrust, therefore the shaft power required to operate the BLI fan will be smaller. In this study, the three C_{fx} targets represent BLI fans on the higher and the lower ends of the spectrum in terms of thrust.

We optimize for three different FPR values at each net force target. In previous work by Gray [9], the optimized designs achieved FPR values on the lower end of the spectrum we consider here, closer to 1.25. This is expected, as the adiabatic efficiency of the fan model increases with decreasing FPR. However, the trade between shaft power and FPR is not straightforward. By optimizing for higher FPR values, we quantify the amount of additional shaft power required to achieve the same net force on the body, if the designs were to use a BLI fan with higher FPR.

IV. Results

All optimizations but one either converged successfully or quit due to numerical difficulties at a feasible point, where the constraints were satisfied to a feasibility tolerance of 10^{-4} . The only case that did not finish successfully is

[‡]<https://github.com/mdolab/pyoptsparse>, accessed May 2019

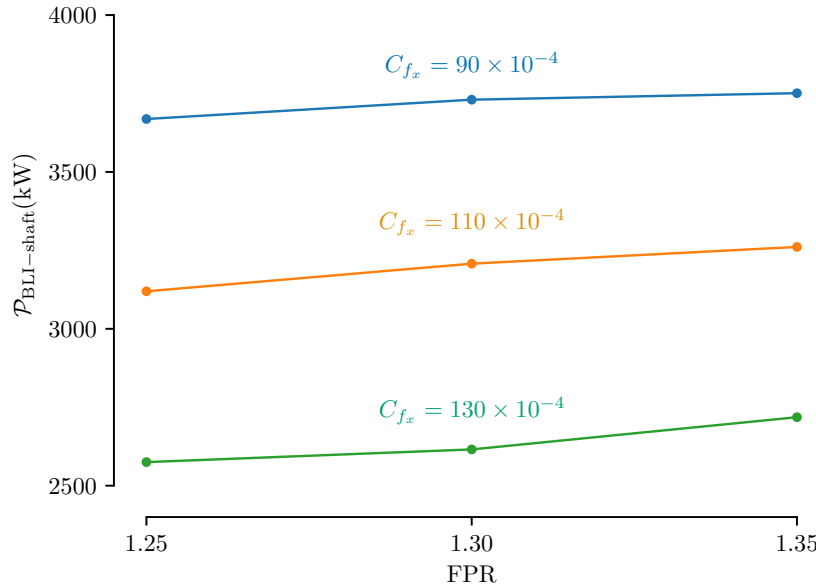


Fig. 8 Required shaft power for optimized results. The sensitivity of shaft power to FPR stays constant across the design space.

the design with $C_{fx} = 90 \times 10^{-4}$ and FPR = 1.30; this was caused by repeated failures in the CFD solver convergence. For this case, we use an intermediate result that was closest to achieving a feasible design. Furthermore, we detail the technical difficulties that arise with these optimization formulations in Appendix A.

The optimized designs show that the shaft power required to operate the BLI fan increases with increasing FPR. Similarly, more power is required to operate the BLI fan for designs where a larger portion of the total thrust is obtained from it, which is equivalent to having a lower C_{fx} value, as demonstrated in Figure 8. Furthermore, the sensitivity of power requirement to FPR is similar across the design space. This behavior shows that the design space is continuous and well behaved for such a BLI system. Table 3 lists the shaft power requirements, along with the relative changes in shaft power compared to the baseline FPR value of 1.25 for all C_{fx} targets. These results show that even though the sensitivity of power requirement to FPR is similar across C_{fx} values, the cases with larger C_{fx} targets, i.e., smaller BLI fans, encounter a more significant relative increase in power compared to the cases with smaller C_{fx} targets.

Secondly, the nacelle diameters decrease with increasing C_{fx} targets for the FPR value of 1.25, as shown in Figure 9. This trend is expected, since a larger C_{fx} target means that the thrust requirement from the BLI fan is decreased. Moreover, Figure 9 demonstrates that the initial design of the nacelle is not optimal, and despite having different diameters, all designs converged to very similar nacelle shapes. In particular, the inlet shape of the nacelle changed considerably compared to the baseline in all optimized designs. These trends show that design studies with the baseline

Table 3 Shaft power requirements in kW for the BLI thruster. The relative increase in power requirements with increasing FPR is greater for larger C_{fx} values, i.e., smaller BLI fans.

| | | C_{fx} | | | | | |
|-----|------|------------------------|--------------|------------------------|--------------|------------------------|--------------|
| | | 90×10^{-4} | | 110×10^{-4} | | 130×10^{-4} | |
| FPR | 1.25 | $P_{BLI\text{-shaft}}$ | $\Delta(\%)$ | $P_{BLI\text{-shaft}}$ | $\Delta(\%)$ | $P_{BLI\text{-shaft}}$ | $\Delta(\%)$ |
| | 1.30 | 3668.7 | 0.0 | 3119.5 | 0.0 | 2575.1 | 0.0 |
| | 1.35 | 3730.3 | 1.7 | 3207.6 | 2.8 | 2615.6 | 1.6 |

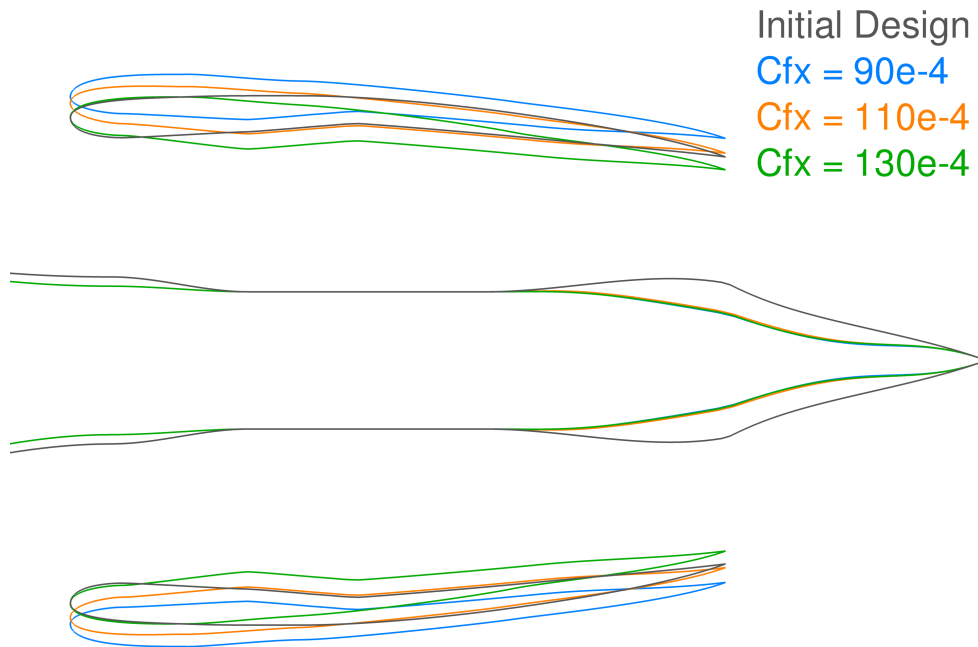


Fig. 9 Outlines of optimized designs on the symmetry plane. The nacelle size is inversely proportional to the C_{fx} target. While all optimized designs converged to similar shapes, the inlet design changed considerably compared to the baseline.

OpenVSP model would yield higher shaft power requirements, whereas design optimization is likely to represent more accurate performance figures for the BLI system.

Similar trends with respect to nacelle sizing can be observed with the rest of the FPR values, as shown in Figure 10, which also contains the stagnation pressure contours normalized with the free-stream static pressure on the symmetry plane. At a free-stream Mach number of 0.785, the ratio between free-stream total pressure and static pressure is about 1.5. In this figure, we plot the areas where the total pressure is higher than the free-stream total pressure with red, while areas that have a lower total pressure are highlighted with blue. This color map demonstrates the effects caused by the wake of the fuselage and the power added to the flow by the BLI fan.

A portion of the BLI power savings is achieved by minimizing the energy lost in the wake of the aircraft [3]. In this context, the wake of a non-boundary layer ingesting propulsor and a fuselage would have non-uniformities in the velocity profile. With the color map we introduced here, this would appear with regions of red behind the propulsor where the jet velocity is higher than free stream, and regions of blue behind the fuselage where the flow velocity is lower due to the viscous losses. BLI reduces the power requirements by reducing these non-uniformities in the wake, i.e., as the BLI fan ingests the fuselage boundary layer, it generates a more uniform velocity distribution in the wake, therefore reducing the amount of energy lost in the wake.

With this concept in mind, we can see that designs with higher FPR targets show a greater non-uniformity at the nacelle exit, whereas designs with lower FPR values show a more uniform total pressure distribution, as shown in Figure 10. Despite the required shaft power being more sensitive to the target C_{fx} than FPR, the total pressure distribution on the nacelle exit is more sensitive to the target FPR than C_{fx} . The non-uniform total pressure distributions represent designs where more energy is lost in the wake of the aircraft, therefore these results support the design intuition that fans with a lower FPR is more suitable for BLI applications.

The nacelle inlet size and the total pressure distribution on the fan face are important factors in BLI fan design. While the nacelle inlet size is a direct representation of the physical size of the BLI system, the total pressure distribution on the fan face demonstrates how much of the boundary layer is ingested by the fan. With a larger nacelle inlet, the fan can ingest more of the boundary layer generated by the fuselage; however, this introduces a weight penalty on the design. Furthermore, nacelles with very large diameters end up taking in some flow directly from the free stream, rather than the wake of the fuselage. This is not desirable, since it introduces more non-uniformity on the fan-face total pressure distribution, which in return causes more inlet distortion and the fan to be heavier due to material fatigue constraints.

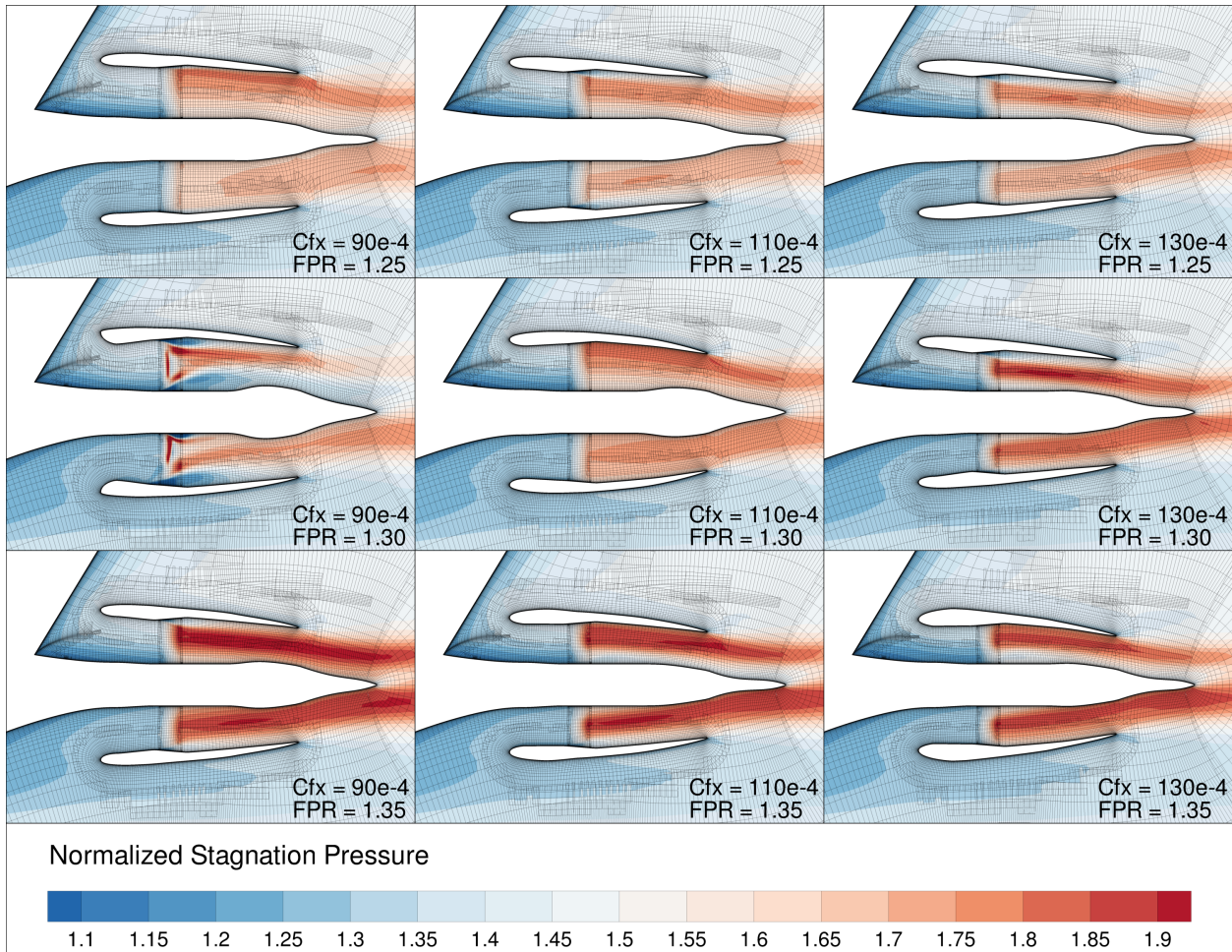


Fig. 10 Optimized designs viewed from the symmetry plane. Higher FPR values yield more non-uniformity in the total pressure distribution in the aircraft wake.

These concepts can be observed by visualizing the total pressure distribution on the fan face.

Figure 11 plots the normalized total pressure contours on the fan faces, along with the nacelle inlet shapes. We can see that the lower C_{fx} and FPR targets resulted in the largest nacelle inlet diameter, while the smallest diameter is obtained with the largest C_{fx} and FPR values. On top of the trend we see for fixed FPR values, these results also demonstrate how the fan size gets smaller as FPR increases for a constant C_{fx} target. Furthermore, while larger fans resulted in a circular design, the smaller fans start to show deviations from the initial axi-symmetric design, where the aspect ratio of the nacelle inlet is modified and the inlet is no longer circular.

Figure 11 also shows that the effects of the wake are more pronounced on the lower side of the BLI nacelle, compared to the upper side. This result is counter-intuitive, because we would expect the top side of the fuselage to have a stronger effect on this distribution due to the vertical tail. To visualize the source of the wake on the lower side of the nacelle, we plot the iso-surfaces of normalized stagnation pressure in Figure 12 using the optimized design for $C_{fx} = 90 \times 10^{-4}$ and FPR = 1.25. Here, we used the same color map we used in Figures 10 and 11. The values we plot, which are all below the free-stream value of 1.5, demonstrate the areas where stagnation pressure is lower than the free stream stagnation pressure.

The iso-surfaces and streamlines in Figure 12 show that the source of lower stagnation pressure on the bottom side of the aircraft is caused by interactions between the fuselage and the downwash from the wing. This result suggests that more BLI benefits can be achieved if the BLI fan is allowed to move in the vertical direction with respect to the fuselage; however, constraints on rotation angle and tail clearance during takeoff limit this change. Furthermore, fan-face distortion can be reduced by introducing additional shape design variables that control the geometry of the rear fuselage.

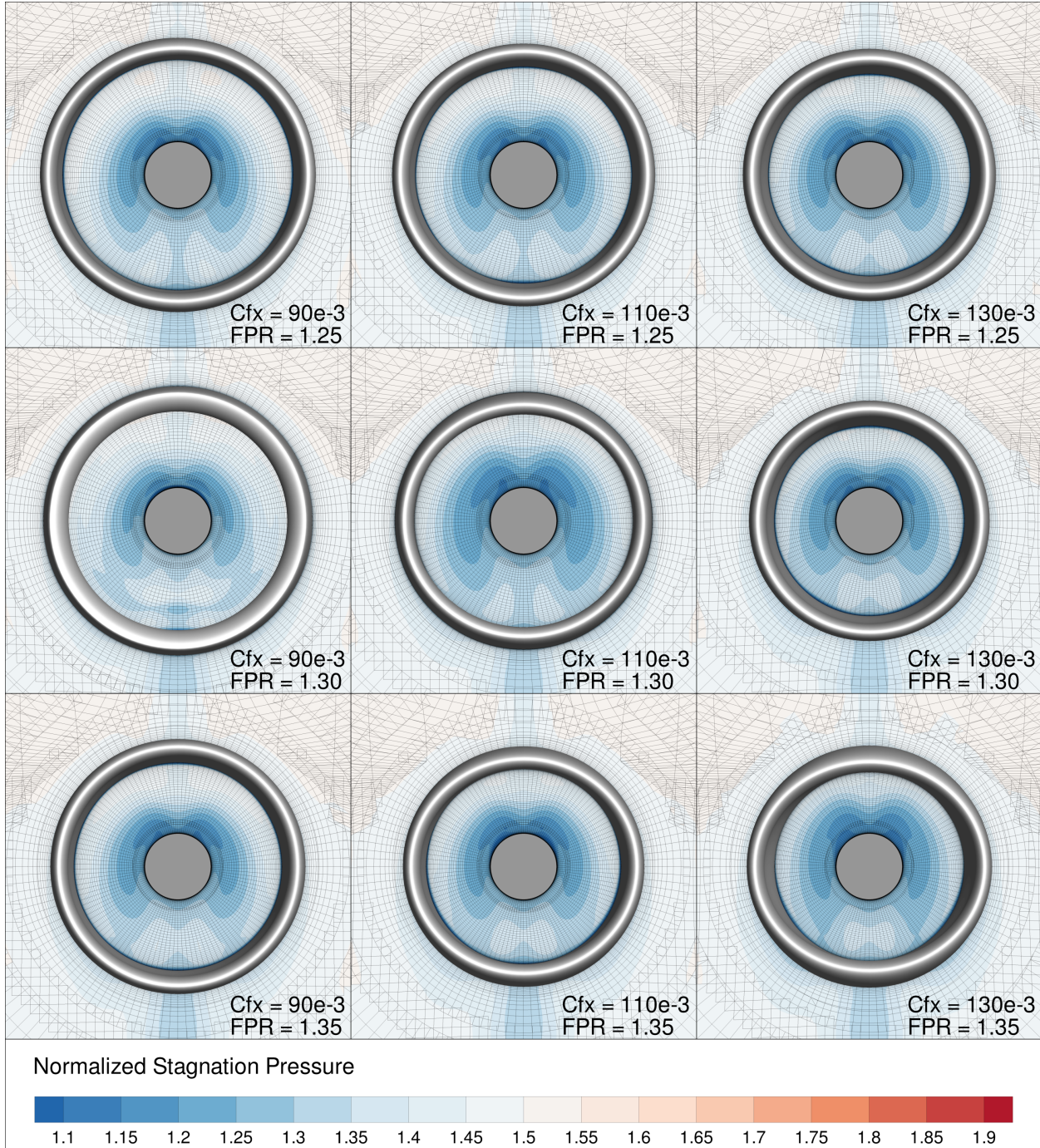


Fig. 11 Stagnation pressure distributions on the fan face, along with the optimized nacelle shapes. The plots demonstrate the trends in nacelle size with respect to C_{fx} and FPR targets. Most designs converged to a circular nacelle, while the smaller nacelles deviated from the circular inlet for an elliptical one.

V. Conclusions

In this work, we studied the BLI system design of the STARC–ABL concept. We described our coupled aeropropulsive framework and performed nine aeropropulsive design optimizations to minimize the shaft power required to operate the BLI fan at a range of net force coefficient and FPR values. The results show that BLI fans that operate at higher FPR values require more shaft power as expected. Similarly, the cases with lower net force coefficients, where the BLI fan is

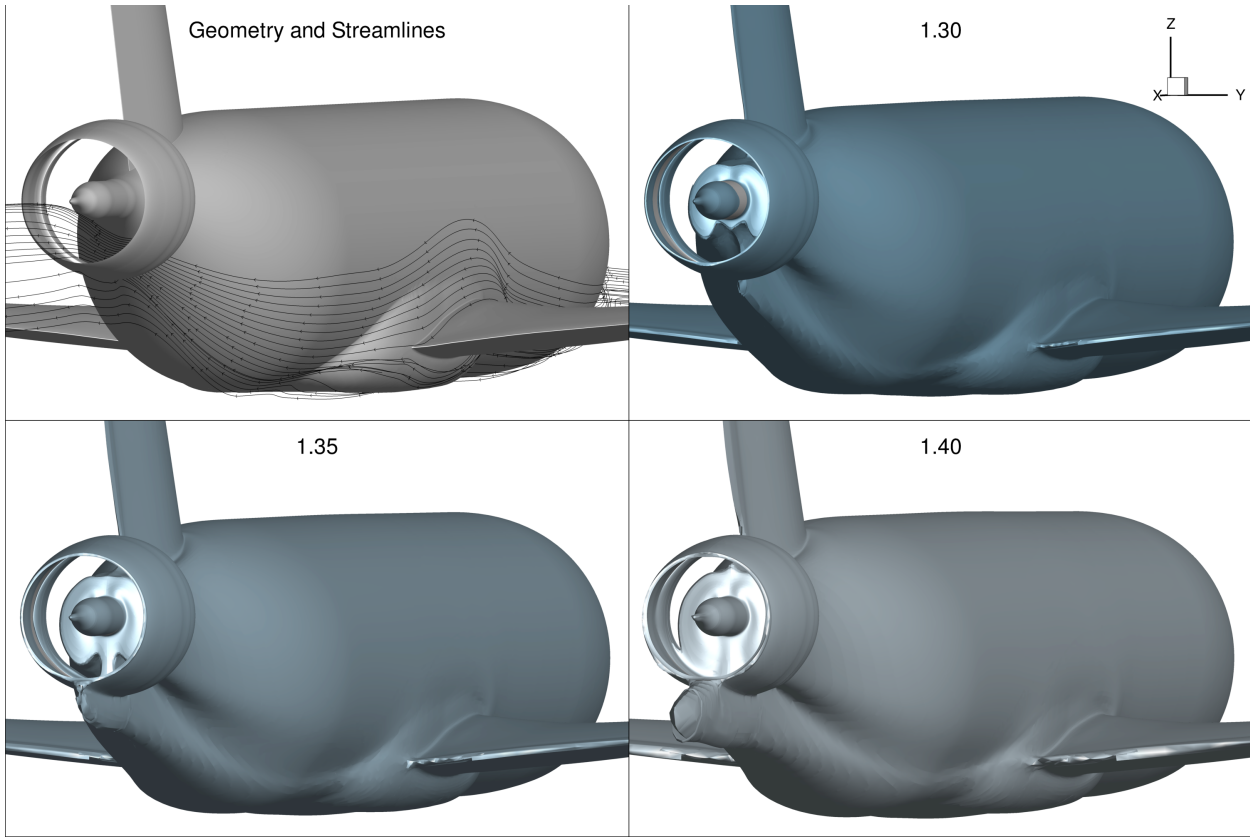


Fig. 12 Iso-surfaces of normalized stagnation pressure. The values for iso-surfaces are listed at the top of each frame. The top left frame shows the geometry without any iso-surface, along with the streamlines that pass through the lower side of the BLI nacelle. Interactions between the fuselage and downwash from the wing cause a large area with lower stagnation pressure on the bottom side of the aft fuselage.

responsible for a larger proportion of the total thrust, required more shaft power to operate the BLI fan.

The trends suggest that the sensitivity of shaft power requirement to FPR does not change greatly across the design space. However, compared to the baseline power requirements at the FPR value of 1.25, smaller BLI fans, i.e., designs with larger C_{f_x} values, encounter a larger relative power penalty for an increase in FPR, whereas the larger fans that require more shaft power are not affected from a higher FPR value as much.

Despite BLI fan shaft power being more sensitive to the target C_{f_x} rather than FPR, the non-uniformity in total pressure distribution at the BLI nacelle exit is more sensitive to FPR. Since BLI aims to improve aeropropulsive efficiency by reducing the amount of energy wasted in the aircraft wake, this trend suggests that fans with a smaller FPR is more suitable for BLI applications.

We observe that despite having different diameters, the optimal nacelle shapes converged to similar designs for the same FPR value and a range of C_{f_x} values. These nacelle shapes are especially different from the baseline design at the inlet. This suggests that if design studies only considered changes in the propulsion system and used the baseline geometry, the results would require a higher shaft power because the initial design is suboptimal. Therefore, aeropropulsive design optimization is required for a more realistic design study of the STARC-ABL concept.

Finally, we demonstrated how the interactions between the fuselage and the downwash from the wings cause non-uniformities in the aircraft wake. This creates a large area with lower stagnation pressure around the bottom side of the rear fuselage, compared to the free-stream value. To increase the power savings with BLI by ingesting the low-speed flow in this region, the BLI fan can be allowed to shift in the vertical direction with respect to the fuselage; however, this would require including constraints on rotation angle and tail clearance during takeoff. Furthermore, design of the rear fuselage can be optimized to reduce the fan-face distortion.

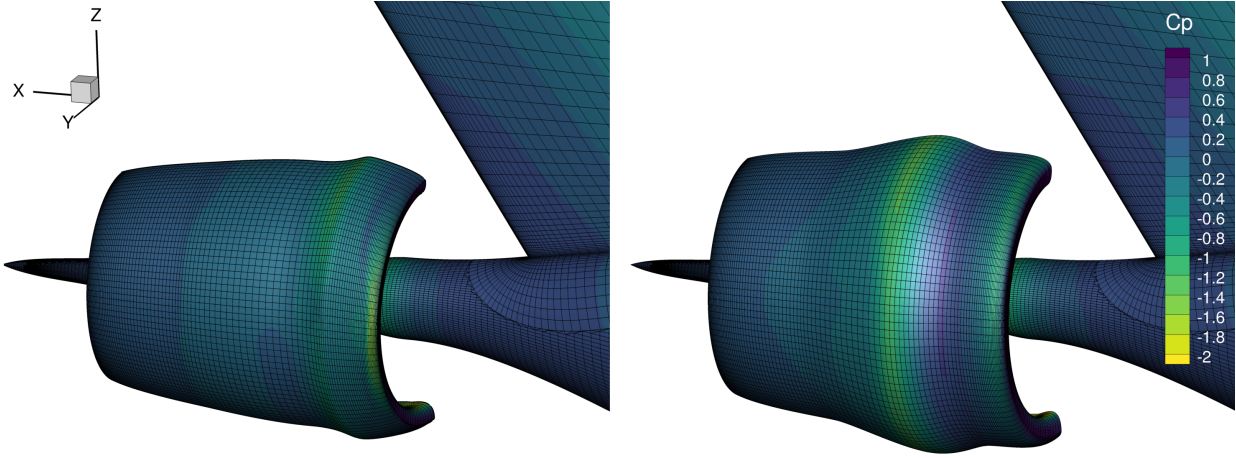


Fig. 13 Two of the infeasible intermediate designs, where the optimizer tried increasing separation to match the net force constraint.

Appendix

A. Technical Challenges

Even though we present results from nine optimizations herein, the robustness of the optimization process as a whole needs to be improved for more detailed studies using the current framework. In this section, we list the difficulties we faced while performing these design optimizations and how we solved or plan on solving these issues.

The biggest technical challenge while optimizing a configuration that uses BLI, is the pitfalls caused by the initial design selection. Because the traditional thrust and drag accounting schemes fall apart with the introduction of BLI, we need to impose total net force constraints on the whole aircraft. This is done through the constraint on C_{fx} herein. To minimize the shaft power, the optimizer will converge to a design that reduces separation to minimize viscous losses, while minimizing the amount of thrust required by the BLI fan. However, this trade is not clear for the optimizer during the initial stages of optimizations, and depending on the initial design, these two effects can lead to very different outcomes in the optimization process.

The initial design requires an initial value for the fan model thrust used in the CFD simulations. If this thrust value is low enough so that the C_{fx} value is above the target, i.e., more thrust is required to achieve the net force constraint, the optimizations progress more smoothly by increasing the BLI thrust to satisfy the C_{fx} constraint. However, if the initial thrust is selected to be too high, the initial C_{fx} value ends up being lower than the target, i.e., the net force needs to be increased in the x direction. This can be achieved either by reducing thrust, or increasing the amount of viscous losses. While a human designer would intuitively reduce the thrust for this scenario, the optimizer might try to match the C_{fx} constraint by introducing separation to increase viscous losses. This might seem counter-intuitive, but these optimization problems are very complex, and the scaling of the design variables and constraints might push the optimizer towards this direction. Even though we would expect the optimizer to ultimately overcome this challenge and converge to the optimal design, the CFD solver usually fails with these extreme cases, and therefore, causes the optimization process to stall. Figure 13 shows two examples where the optimizer modified the nacelle shape to introduce separation. We can avoid this behavior with an initial thrust value that yields a higher C_{fx} value compared to the target.

Another challenge with the optimizations is the CFD solver convergence. Yildirim et al. [16] developed a robust, Jacobian-free approximate Newton–Krylov (ANK) solver for aerodynamic shape and multidisciplinary design optimization in mind. Despite being the most robust option in ADflow, this solver was tuned for either aerodynamic, or aerostructural simulations. As a result, aeropropulsive simulations like we perform herein cause convergence issues with the solver, and solver robustness needs to be improved for further aeropropulsive design studies.

The remaining failures are due to the parametrization of design variables. As we introduced in Section II.A, we use human readable design variables in this work. While we need large bounds on these variables to avoid restricting the design space, certain combinations of these design variables cause unfeasible geometries, as shown in Figure 14. These cases ultimately cause the volume mesh warping algorithm to fail. To avoid these failures, we need to define improved

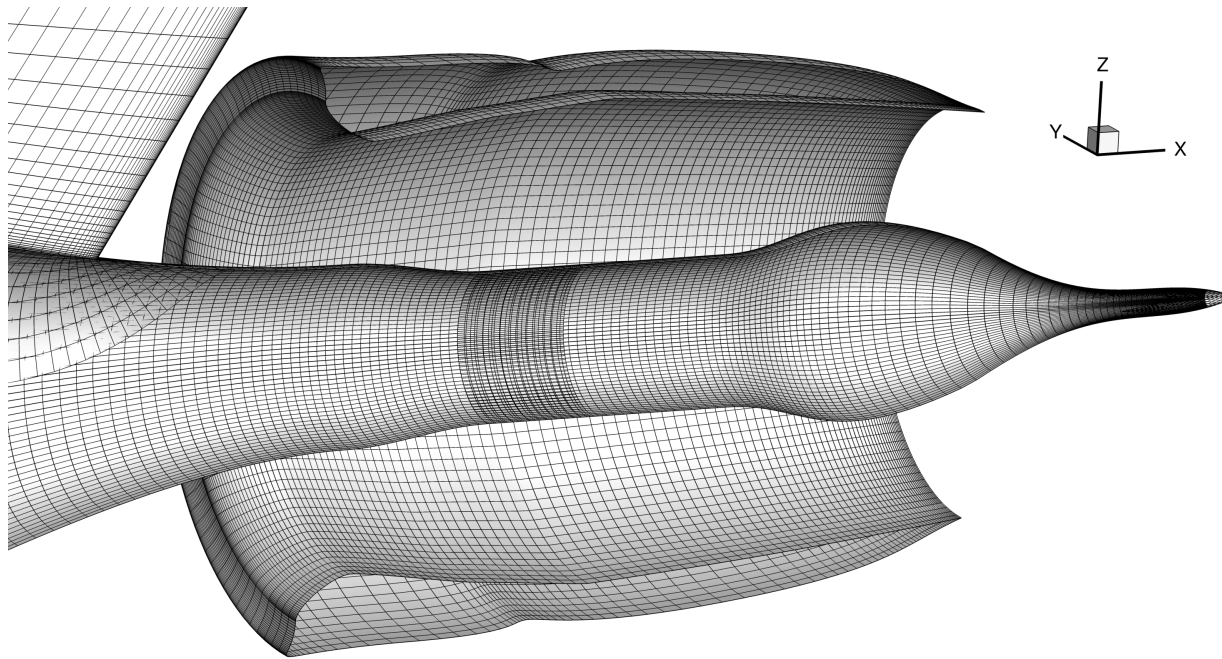


Fig. 14 Certain combinations of geometry design variables may create irregularities in the nacelle design, that ultimately cause the volume mesh warping algorithm to fail.

design variables that do not restrict the designs space while keeping the designs themselves reasonable.

Acknowledgments

This work was funded by the NASA Advanced Air Transport Technology (AATT) and Transformational Tools and Technologies (TTT) projects. Computational resources were provided by the NASA High-End Computing (HEC) Program through the NASA Advanced Supercomputing (NAS) Division at Ames Research Center, and the Extreme Science and Engineering Discovery Environment (XSEDE), which is supported by the National Science Foundation grant number ACI-1548562. Special thanks to Dr. Gaetan Kenway for his technical support.

References

- [1] Uranga, A., Drela, M., Hall, D. K., and Greitzer, E. M., "Analysis of the Aerodynamic Benefit from Boundary Layer Ingestion for Transport Aircraft," *AIAA Journal*, Vol. 0, No. 0, 2018, pp. 1–11. doi:10.2514/1.J056781.
- [2] Smith, J., Leroy, "Wake ingestion propulsion benefit," *27th Joint Propulsion Conference*, American Institute of Aeronautics and Astronautics, 1991. doi:10.2514/6.1991-2007.
- [3] Drela, M., "Power Balance in Aerodynamic Flows," *AIAA Journal*, Vol. 47, No. 7, 2009, pp. 1761–1771. doi:10.2514/1.42409.
- [4] Welstead, J., and Felder, J. L., "Conceptual Design of a Single-Aisle Turboelectric Commercial Transport with Fuselage Boundary Layer Ingestion," *54th AIAA Aerospace Sciences Meeting*, American Institute of Aeronautics and Astronautics, 2016. doi:10.2514/6.2016-1027.
- [5] Hall, D. K., Greitzer, E. M., and Tan, C. S., "Analysis of Fan Stage Conceptual Design Attributes for Boundary Layer Ingestion," *Journal of Turbomachinery*, Vol. 139, No. 7, 2017, pp. 071012–071012–10. doi:10.1115/1.4035631.
- [6] Gray, J. S., and Martins, J. R. R. A., "Coupled Aeropropulsive Design Optimization of a Boundary Layer Ingestion Propulsor," *The Aeronautical Journal*, Vol. 123, No. 1259, 2019, pp. 121–137. doi:10.1017/aer.2018.120.

- [7] Gray, J. S., Kenway, G. K. W., Mader, C. A., and Martins, J. R. R. A., "Aero-propulsive Design Optimization of a Turboelectric Boundary Layer Ingestion Propulsion System," *2018 AIAA/ISSMO Multidisciplinary Analysis and Optimization Conference*, Atlanta, GA, 2018. doi:10.2514/6.2018-3976, aIAA 2018-3976.
- [8] Kenway, G. K., and Kiris, C. C., *Aerodynamic Shape Optimization of the STARC-ABL Concept for Minimal Inlet Distortion*, American Institute of Aeronautics and Astronautics, 2018. doi:10.2514/6.2018-1912.
- [9] Gray, J., "Design Optimization of a Boundary Layer Ingestion Propulsor Using a Coupled Aeropropulsive Model," Ph.D. thesis, University of Michigan, 2018. doi:2027.42/147625.
- [10] Gray, J. S., Mader, C. A., Kenway, G. K. W., and Martins, J. R. R. A., "Modeling Boundary Layer Ingestion Using a Coupled Aeropropulsive Analysis," *Journal of Aircraft*, Vol. 55, No. 3, 2018, pp. 1191–1199. doi:10.2514/1.C034601.
- [11] Gray, J. S., Hwang, J. T., Martins, J. R. R. A., Moore, K. T., and Naylor, B. A., "OpenMDAO: An open-source framework for multidisciplinary design, analysis, and optimization," *Structural and Multidisciplinary Optimization*, Vol. 59, No. 4, 2019, pp. 1075–1104. doi:10.1007/s00158-019-02211-z.
- [12] Hahn, A., "Vehicle Sketch Pad: A Parametric Geometry Modeler for Conceptual Aircraft Design," *48th AIAA Aerospace Sciences Meeting Including the New Horizons Forum and Aerospace Exposition*, American Institute of Aeronautics and Astronautics, 2010. doi:10.2514/6.2010-657.
- [13] Secco, N. R., Jasa, J. P., Kenway, G. K. W., and Martins, J. R. R. A., "Component-based Geometry Manipulation for Aerodynamic Shape Optimization with Overset Meshes," *AIAA Journal*, Vol. 56, No. 9, 2018, pp. 3667–3679. doi:10.2514/1.J056550.
- [14] Luke, E., Collins, E., and Blades, E., "A Fast Mesh Deformation Method Using Explicit Interpolation," *Journal of Computational Physics*, Vol. 231, No. 2, 2012, pp. 586–601. doi:10.1016/j.jcp.2011.09.021.
- [15] Kenway, G. K. W., Mader, C. A., He, P., and Martins, J. R. R. A., "Effective Adjoint Approaches for Computational Fluid Dynamics," *Progress in Aerospace Sciences*, 2019. (Submitted).
- [16] Yildirim, A., Kenway, G. K. W., Mader, C. A., and Martins, J. R. R. A., "A Jacobian-free approximate Newton–Krylov startup strategy for RANS simulations," *Journal of Computational Physics*, 2018. (Submitted).
- [17] Gray, J. S., Chin, J., Hearn, T., Hendricks, E., Lavelle, T., and Martins, J. R. R. A., "Chemical Equilibrium Analysis with Adjoint Derivatives for Propulsion Cycle Analysis," *Journal of Propulsion and Power*, Vol. 33, No. 5, 2017, pp. 1041–1052. doi:10.2514/1.B36215.
- [18] Jasa, J. P., Gray, J. S., Seidel, J. A., Mader, C. A., and Martins, J. R. R. A., "Multipoint Variable Cycle Engine Design Using Gradient-based Optimization," *57th AIAA Aerospace Sciences Meeting, AIAA SciTech Forum, 2019*, San Diego, CA, 2019. doi:10.2514/6.2019-0172.
- [19] Lambe, A. B., and Martins, J. R. R. A., "Extensions to the Design Structure Matrix for the Description of Multidisciplinary Design, Analysis, and Optimization Processes," *Structural and Multidisciplinary Optimization*, Vol. 46, 2012, pp. 273–284. doi:10.1007/s00158-012-0763-y.
- [20] Gill, P. E., Murray, W., and Saunders, M. A., "SNOPT: An SQP algorithm for large-scale constrained optimization," *SIAM Journal of Optimization*, Vol. 12, No. 4, 2002, pp. 979–1006. doi:10.1137/S1052623499350013.
- [21] Perez, R. E., Jansen, P. W., and Martins, J. R. R. A., "pyOpt: A Python-Based Object-Oriented Framework for Non-linear Constrained Optimization," *Structural and Multidisciplinary Optimization*, Vol. 45, No. 1, 2012, pp. 101–118. doi:10.1007/s00158-011-0666-3.